

Optomechanical realization of the bosonic Kitaev-Majorana chain

Jesse J. Slim,^{1,2} Clara C. Wanjura,³ Matteo Brunelli,⁴ Javier del Pino,^{5,1} Andreas Nunnenkamp,⁶ and Ewold Verhagen^{1,*}

¹*Center for Nanophotonics, AMOLF, Science Park 104, 1098 XG Amsterdam, The Netherlands*

²*ARC Centre of Excellence for Engineered Quantum Systems,*

School of Mathematics and Physics, University of Queensland, St. Lucia, QLD 4072, Australia.

³*Max Planck Institute for the Science of Light, Staudtstraße 2, 91058 Erlangen, Germany*

⁴*Department of Physics, University of Basel, Klingelbergstrasse 82, 4056 Basel, Switzerland*

⁵*Institute for Theoretical Physics, ETH Zürich, 8093 Zürich, Switzerland*

⁶*Faculty of Physics, University of Vienna, Boltzmannngasse 5, 1090 Vienna, Austria*

The fermionic Kitaev chain is a canonical model featuring topological Majorana zero modes. We report the experimental realization of its bosonic analogue in a nano-optomechanical network where parametric interactions induce two-mode squeezing and beamsplitter coupling among the nanomechanical modes, equivalent to hopping and superconductor pairing in the fermionic case, respectively. We observe several extraordinary phenomena in the bosonic dynamics and transport, including quadrature-dependent chiral amplification, exponential scaling of the gain with system size, and strong sensitivity to boundary conditions. Controlling the interaction phases and amplitudes uncovers a rich dynamical phase diagram that links the observed phenomena to non-Hermitian topological phase transitions. Finally, we present an experimental demonstration of an exponentially enhanced response to a small perturbation as a consequence of non-Hermitian topology. These results represent the demonstration of a novel synthetic phase of matter whose bosonic dynamics do not have fermionic parallels, and establish a powerful system to study non-Hermitian topology and its applications in signal manipulation and sensing.

Topological phases of matter have revolutionized our understanding of electronic materials [1] and classical wave systems [2, 3], with unique applications in robust information transmission, metrology, and quantum computing [4, 5]. Intense interest focused recently on topological phenomena in metamaterials that feature non-Hermitian dynamics — associated with amplification and dissipation that are ubiquitous in bosonic domains such as photonics and acoustics [6, 7]. On the one hand, there is the fundamental question of how to recognize and classify non-Hermitian topological phases. Indeed, whereas topological invariants in Hermitian systems are usually defined on the structure of their eigenvectors [1], non-Hermitian systems can additionally be classified on the structure of their complex eigenvalues [8–10]. On the other hand, the merger of non-Hermitian dynamics and topology may lead to new physical phenomena, and associated applications from robust lasing and topologically protected amplification to enhanced sensing [11–13]. A widely studied phenomenon is the non-Hermitian skin effect (NHSE); the accumulation of a macroscopic number of states at boundaries of non-Hermitian lattices [14–19]. This was observed experimentally in various systems [20–27] and seemingly violates the bulk-boundary correspondence that famously links the existence of robust edge states to the topological description of a material’s bulk properties in Hermitian topological insulators.

Against this backdrop, McDonald et al. recently proposed the bosonic Kitaev-Majorana chain (BKC) [28]. It is a bosonic analogue of the fermionic Kitaev chain

— the well-known one-dimensional model that predicts topologically-protected Majorana zero modes at the ends of a superconducting wire [29]. The BKC is formed by coupling bosonic modes through both beamsplitter and two-mode squeezing interactions, mimicking hopping and p -wave superconducting pairing in the fermionic Kitaev chain, respectively (Fig. 1). While the BKC lacks the fermionic statistics that make Majorana bound states interesting to quantum computing [4, 5], it hosts a set of remarkable features, that also set it apart from other metamaterial networks [30, 31]. These features include quadrature-dependent chiral transport and amplification, and strong sensitivity to boundary conditions which can be connected to its non-Hermitian topological properties [28, 32]. The BKC has been predicted to offer sensing applications due to an exponential boost of sensitivity to signals perturbing the end of the chain [33], and metastable states at the chain ends have been described as bosonic Majorana zero modes [34]. All of these traits establish the BKC as a highly interesting non-Hermitian topological phase of matter.

Optomechanical resonator chain

We realize the bosonic Kitaev-Majorana chain experimentally in an actively controlled classical optomechanical network, study the rich dynamical behavior that ensues, and link it to the system’s non-Hermitian topology. The nodes of the one-dimensional chain are the flexural nanomechanical modes of a pair of silicon strings (Fig. 1a,c) with different resonance frequencies $\omega_j/(2\pi)$ ranging between 3.7 and 26 MHz. The displacements of

* verhagen@amolf.nl

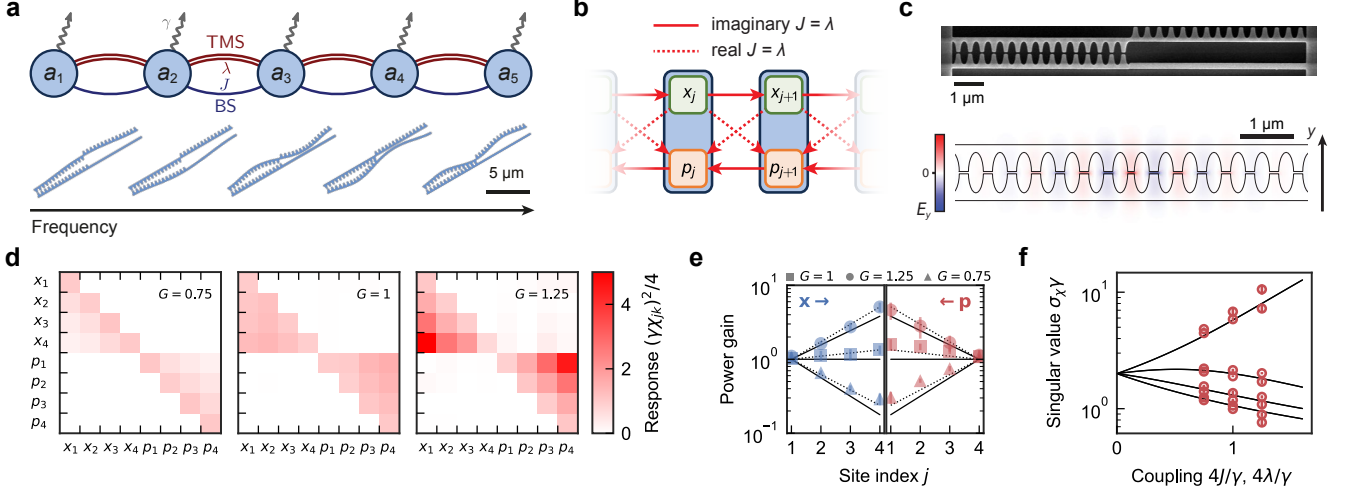


FIG. 1. **Bosonic Kitaev-Majorana Chain (BKC) in an optomechanical network.** (a) The BKC comprises resonators coupled through beamsplitter (BS) and two-mode squeezing (TMS) interactions. The mechanical displacement profiles of the modes that form the sites of the chain are depicted below. (b) By tuning the phases of BS and TMS amplitudes, specific quadratures can be coupled in a unidirectional fashion for $|J| = |\lambda|$. (c) SEM micrograph of the sliced photonic crystal nanobeam system (top) and simulated electric field in the nanocavity that is coupled to the mechanical modes (bottom). The time-modulated cavity field induces all parametric interactions. (d) Susceptibility matrix χ_{jk} resolved in the resonator quadratures along the chain for purely imaginary $J = \lambda = i\mu$. As the per-link gain $G = 4\mu/\gamma$ increases, the system features quadrature-dependent chiral end-to-end amplification. (e) Concomitantly, the chain builds up exponential gain along the decoupled chains of x_j and p_j quadratures. The expected gain profiles for the nominal values of G noted above are shown (solid lines). A closer agreement is obtained after including a correction of +5% on all interaction rates (dashed lines). (f) Singular values σ_χ of the susceptibility matrices in (d) as a function of G , corresponding to gain of the various transmission channels. The emerging separation between two (amplifying) singular values and the remaining ones with much smaller gain can be associated with a non-Hermitian bulk-boundary correspondence. Error bars represent $\pm 2\sigma$ with σ the standard deviation obtained by repeating each experiment 10 times.

all mechanical modes affect the optical frequency of a single photonic nanocavity defined in the nanoscale gap between the strings by the sliced photonic crystal geometry [35, 36]. This optomechanical coupling implies that radiation pressure of a drive laser that is coupled to the cavity from free space and tuned to the side of the cavity resonance (linewidth $\kappa/2\pi = 320$ GHz) induces a strong optomechanical spring effect, as the optical force adiabatically follows mechanical displacement (in the ‘bad cavity’ regime, $\kappa \gg \omega_j$). Temporal modulation of the laser intensity then yields control over the nanomechanical interaction Hamiltonian through parametric driving: Beamsplitter (BS) interactions between modes i and j are induced by modulation at the respective frequency difference $|\omega_j - \omega_i|$, and two-mode squeezing (TMS) through sum-frequency modulation at $|\omega_i + \omega_j|$, with each coupling’s rate and phase controlled by the depth and phase of the relevant modulation tone [36–38]. The effective Hamiltonian that we implement reads

$$H_{\text{BKC}} = \sum_j \left(J a_{j+1}^\dagger a_j + \lambda a_{j+1}^\dagger a_j^\dagger + \text{H.c.} \right), \quad (1)$$

with modes described by bosonic annihilation operators a_j in frames rotating at ω_j , and J (λ) the complex BS (TMS) amplitude, set identical on each link of the chain.

While this Hamiltonian is obviously Hermitian, it generates non-Hermitian dynamics in the modes a_j , associated with the particle-non-conserving TMS interactions.

Chiral amplification

We measure the chain’s full response to a modulated radiation pressure drive resonant with any of the modes, by demodulating the induced vibrations detected by a second (readout) laser. Similar to its fermionic counterpart, the BKC is best understood using Hermitian quadrature operators $x_j = (a_j + a_j^\dagger)/\sqrt{2}$ and $p_j = (a_j - a_j^\dagger)/(i\sqrt{2})$. We separately resolve the x and p quadratures [37, 38] in the measured susceptibility matrix χ shown in Fig. 1d, which relates the steady-state amplitudes $\mathbf{q} = (\langle x_1 \rangle, \dots, \langle x_N \rangle, \langle p_1 \rangle, \dots, \langle p_N \rangle)^T$ (in units of zero-point amplitudes $x_{\text{zpf},j}$) to resonant drives of each quadrature $\mathbf{f}^{(\mathbf{q})} = (f_{x_1}, \dots, f_{x_N}, f_{p_1}, \dots, f_{p_N})$ through $\mathbf{q} = \chi \mathbf{f}^{(\mathbf{q})}$ [37]. We choose in Fig. 1d both J and λ to be purely imaginary and equal; $\lambda = J = i\mu$ ($\mu > 0$), and plot χ^2 for $N = 4$ for various values of $G \equiv 4\mu/\gamma$. The damping rates of all modes are equalized to $\gamma_j/(2\pi) = \gamma/(2\pi) = 8$ kHz through measurement-based feedback [37]. Drives are normalized such that

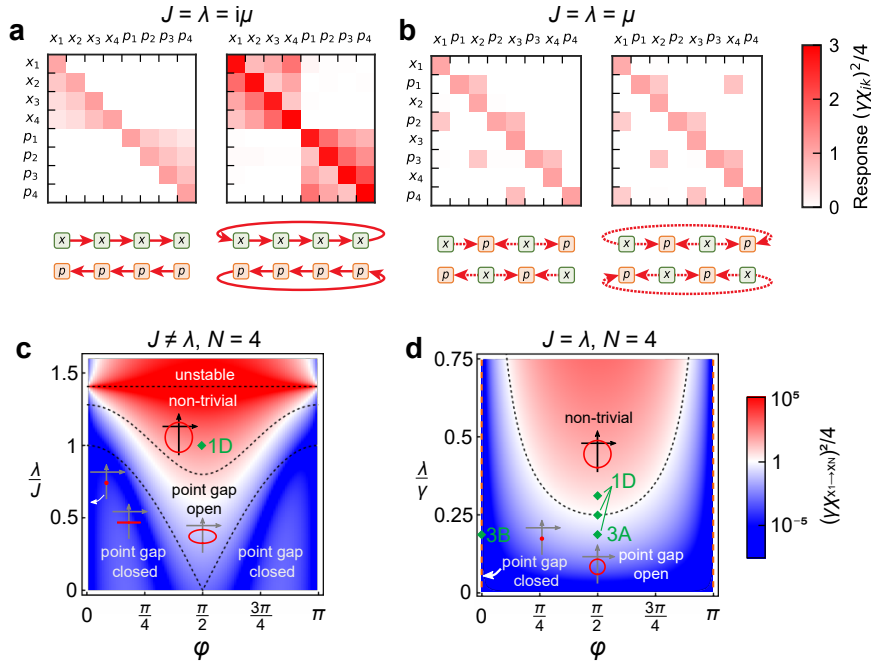


FIG. 3. **Transport properties and topological phase diagrams of generalized bosonic Kitaev-Majorana chains.** (a,b) Measured susceptibility matrices for $N = 4$. In (a) $\lambda = J = i\mu$ for OBC (left) and PBC (right). In (b) $\lambda = J = \mu$ for OBC (left) and PBC (right). In all cases $\mu/(2\pi) = 1.5$ kHz and $\gamma/(2\pi) = 8$ kHz such that $G = 0.75$. The sketches below the panels indicate the quadrature-dependent couplings that underlie the transport behavior. (c) The generalized BKC features four different regimes, distinguished by the spectral structure under PBC: point gap closed, point gap open without spectrally winding the origin, a regime of non-trivial non-Hermitian topology where the spectrum winds the origin, and a fully unstable regime. Dashed lines indicate phase boundaries. The color shows end-to-end gain $\chi_{x_1 \rightarrow x_N}$ in the corresponding open chain as a function of phase φ and λ/J for $J/\gamma = 5/16$ and $N = 4$. (d) For $\lambda = J$ the phase diagram simplifies: The OBC system is guaranteed to be stable and a point gap opens except at $\varphi = 0, \pi$ (red dashed lines). Green diamonds indicate the parameters of the experiments in Figures 1 and 3.

implies the breakdown of the bulk-boundary correspondence that links the number of edge states to the topological invariant [6–8, 17–19, 26, 32, 41–43]. Bulk-boundary correspondence can be restored by specifically considering spectral windings around the origin of the complex plane [43–45]. That winding number acts as a topological invariant that predicts the number of singular values of the non-Hermitian Hamiltonian matrix χ^{-1} that split off from the bulk values and approach zero for large system size [43]. Those zero singular values are directly connected to diverging singular values of the susceptibility χ . The two channels of directional amplification that we recognized in Fig. 1f thus have a topological nature, and can be compared to the zero modes of the fermionic Kitaev-Majorana chain.

At variance with the Hatano-Nelson model, the non-Hermitian topological phase of the BKC is protected by a parity symmetry [10], which also decouples the quadratures and doubles the eigenvalues in eq. 3. This symmetry expresses the fact that the system is invariant under reflection and exchanging x and p [37] (Fig. 1d). Interestingly, the fact that our experiment employs a synthetic dimension means that detuning disorder can be minimized through careful adjustment of the modulation

frequencies. This ensures the symmetry, revealing the non-Hermitian topology and all its implications in our optomechanical BKC.

A distinctive trait of non-Hermitian topological models is sensitivity to boundary conditions. We realize periodic boundary conditions (PBC) in our optomechanical network by connecting also the last node to the first. As the gain exceeds unity, we observe strong increase accompanied by spectral narrowing of the thermal fluctuations that is characteristic of dynamical instability for PBC (Fig. 2). The oscillation amplitude is limited by nonlinearities [37]. In stark contrast, the system under open boundary conditions (OBC) is dynamically stable at the same gain. This boundary-dependent dynamical instability is thus a dramatic feature that coincides for our zero-detuning network with the non-Hermitian topological phase transition that occurs as soon as the complex energies under PBC start to wind the origin [43, 44]. This is a convective instability, i.e. excitations experience net round-trip gain and grow indefinitely around the closed chain. For the open chain, the point gap remains closed and the dynamics stable (Fig. 2): Amplified excitations reach the end of the chain, but cannot reflect [28].

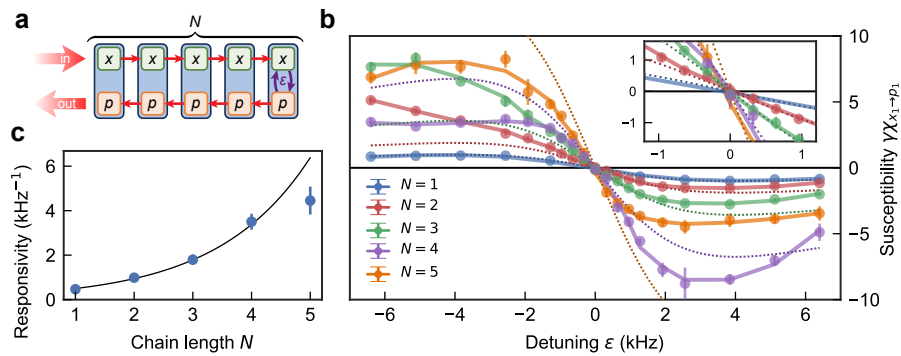


FIG. 4. **Experimental demonstration of exponentially-enhanced sensing.** (a) The response of a BKC comprising N resonators with interactions $J = \lambda = i\mu$ is very sensitive to the local detuning ϵ of the last site. To sense small ϵ , a coherent drive of the first site x_1 gets amplified towards the right. The perturbation ϵ converts a fraction of the excitation to the orthogonal quadrature p_N and gets amplified back towards the first site, where it is detected [33]. The response $\chi_{x_1 \rightarrow p_1}(\epsilon)$ is thus a measure for ϵ , with the chain providing amplification. (b) Susceptibility $\chi_{x_1 \rightarrow p_1}(\epsilon)$ of p_1 to a signal injected in x_1 as a function of ϵ in experiment (circles), with the inset zooming on small ϵ . Here, $\mu/(2\pi) = 2.75$ kHz, $\gamma/(2\pi) = 8$ kHz (per-link gain $G = 1.37$). We attribute the deviation between measured response and linear theory (dashed lines) for large ϵ to nonlinear effects [37]. (c) Linear responsivity \mathcal{R} to small ϵ for increasing N extracted from (b). We observe exponential increase with $N \leq 4$, as predicted by the linear theory (line) using the independently estimated $G = 1.37$. The decreased responsivity for $N = 5$ is attributed to nonlinearity. Error bars represent $\pm 2\sigma$ with σ the standard deviation from 5 experiments.

Topological phase diagram

So far we focused on the choice $\varphi = \pi/2$ for the BS and TMS interactions $J = |J|e^{i\varphi}$ and $\lambda = |\lambda|e^{i\varphi}$, respectively, for which connections to both the fermionic Kitaev-Majorana and non-Hermitian Hatano-Nelson models are most direct. Given the active phase control of our platform, we explore the behavior for different phases φ . Figures 3a,b compare the effect of open or closed boundaries on the response for $\varphi = \pi/2$ and $\varphi = 0$, respectively, in the stable regime ($G = 0.75$). For $\varphi = \pi/2$ the sensitivity to boundary conditions, associated with the opened point gap and NHSE, is clear again: chiral quadrature-dependent transport is terminated at the ends of a finite chain, whereas for PBC signals can circulate continuously, opening transmission to all sites. In contrast, when $\varphi = 0$ (real $J = \lambda$, Fig. 3b), an injected signal only elicits a response in neighboring sites, regardless of boundary conditions. This means that also dynamical stability no longer depends on boundary conditions and the chain is topologically trivial for any G . The behavior can be understood from the fact that x and p quadratures no longer cascade; destructive interference between BS and TMS processes leads to a decoupling of dimers.

In fact, a rich phase diagram emerges as control phases and strengths are varied. As the BKC preserves parity symmetry for all φ , its eigenvalues under PBC always form two degenerate bands in the complex plane. We recognize four distinct dynamical phases in Fig. 3c: The squeezing-induced point gap [46] is opened when $|\lambda| > |J|\cos(\varphi)$. For sufficiently small dissipation, i.e., $\gamma < \sqrt{|\lambda|^2 - |J|^2 \cos^2 \varphi}$, the spectrum winds the origin, marking the topological transition to the non-trivial regime and the boundary-dependent instability that we

observed in Fig. 2. The open chain then functions as a directional amplifier. Chains with open point gap can always be interpreted as two Hatano-Nelson chains of opposite winding, as a transformation maps them for any φ to the case $\varphi = \pi/2$ (with reduced interaction strengths) [28, 37]. In contrast, the regime $|\lambda| < |J|\cos(\varphi)$ is characterized by a closed point gap with eigenstates that are largely insensitive to boundary conditions, and one can map the system to a trivial hopping chain [28, 37]. Finally, also the open chain becomes unstable when $|\lambda/J| > (1 + (\gamma/(2J))^2 \sec^2(\pi N/(1+N)))^{1/2}$.

The phase diagram simplifies in the special case $|\lambda| = |J| = \mu$ (Fig. 3d). The topological phase transition to the directional amplification regime then happens when $2\mu \sin \varphi > \gamma/2$, while the closed point gap region collapses onto lines at $\varphi = 0, \pi$ that are independent of μ . There, all PBC eigenvalues coalesce to a single value $\epsilon_0 = -i\gamma/2$, and the dynamical matrix of a finite closed chain exhibits N degenerate order-2 exceptional points. This special case was probed in Fig. 3b, where we saw that exciting the x quadrature in one site only elicits a p response of its direct neighbors, while $p \rightarrow x$ is forbidden due to destructive interference, an interesting form of quadrature nonreciprocity [37, 38]. In these examples, we see that the BKC's non-Hermitian bandstructure thus links to both its dynamics and transport.

Exponentially-enhanced perturbation responsivity

Unlike the phase φ , a finite detuning on any of the sites breaks the parity symmetry protecting the BKC's non-Hermitian topology [37]. Indeed, detuning a single site, in particular at an edge, significantly alters the re-

sponsivity. This setting has been proposed as a sensor with exponentially-enhanced sensitivity [33].

Fig. 4a illustrates the working principle of a sensor exploiting directional amplification in the BKC, i.e. an N -site open chain with imaginary couplings J, λ . In a non-trivial chain, a signal injected at the x_1 quadrature is amplified to the other end. At the last site, a detuning ε — the quantity to be sensed — converts the excitation in x_N to the orthogonal quadrature p_N . Subsequently, the converted signal is again amplified towards the p_1 quadrature of the first site and detected. Importantly, quadratures x_N and p_N *only* couple due to the presence of the detuning ε . Thus, a measurement of $\chi_{x_1 \rightarrow p_1}$ is highly sensitive to any perturbation that dispersively couples to the last resonator, such as for example the mass of an adhered protein or the state of a qubit coupled to the resonator [33].

We implement the sensing scheme with $J = \lambda = i\mu$ in nanomechanical chains comprising up to 5 sites. A detuning ε at the last site is controlled via tuning of the relevant pump tones, serving as a proxy for a dispersively coupled perturbation. We show the measured response $\gamma\chi_{x_1 \rightarrow p_1}(\varepsilon)$ to a drive of x_1 in Fig. 4b, revealing a strong dependence on ε . We note that the slope of $\gamma\chi_{x_1 \rightarrow p_1}(\varepsilon)$ close to $\varepsilon = 0$ gets steeper for larger system size N (Fig. 4b, inset). We plot this experimentally retrieved linear responsivity [37]

$$\mathcal{R} \equiv \gamma \left. \frac{\partial \chi_{x_1 \rightarrow p_1}}{\partial \varepsilon} \right|_{\varepsilon=0}. \quad (4)$$

as a function of system size in Fig. 4c. Notably, the responsivity grows *exponentially* with the chain length N . We can understand this based on the non-Hermitian topological, directional amplifier (Fig. 1), since in topologically non-trivial phases it displays a susceptibility $|\chi_{x_1 \rightarrow x_N}(\varepsilon = 0)| = |\chi_{p_N \rightarrow p_1}(\varepsilon = 0)| \propto e^{\alpha N}$ with some $\alpha > 1$, that scales exponentially with system size [32, 33]. Concretely [37], the back-and-forth amplification mechanism implies $\mathcal{R} = \gamma[\chi_{x_1 \rightarrow x_N}(\varepsilon = 0)]^2$. Crucially, a point gap is not sufficient for exponential enhancement; it *only* occurs for non-trivial winding number as $\chi_{x_1 \rightarrow x_N}$ is exponentially attenuated otherwise [37]. For equal coupling strengths, the responsivity takes on the simple form $\mathcal{R} = 4G^{2(N-1)}/\gamma$.

For large ε or large total gain, the increased amplitude in the chain prompts non-linear effects that introduce additional detunings and saturate the per-link gain, due to a relatively strong optomechanical nonlinearity [37].

This causes deviation from linear theory in Fig. 4b and a slightly smaller than predicted enhanced sensitivity for $N = 5$ in Fig. 4c. The effect of potential (non-linear) detuning on other sites than the sensing site will be interesting to study in depth in light of practical sensor implementations. Likewise, while effective enhancement of quantum Fisher information through the demonstrated mechanism has been predicted [33], careful evaluation of the contributions of thermal or quantum fluctuations should be the subject of future work.

Conclusions and outlook

These results point to potential applications of the BKC in sensing and directional amplification, which are both related to its behavior as a unique non-Hermitian topological phase. Many more directions of study are opportune: characterizing the properties of the chain's Majorana zero modes [34], exploring the inclusion of nonlinearity and associated 'fermionization' of the system [47], extension to higher dimensions, and studying non-Hermitian braiding operations [48, 49]. We have experimentally shown that the BKC constitutes a non-Hermitian topological model that unifies the concepts of spectral winding, the non-Hermitian skin effect, and directional amplification, with different topological phases linked to observable effects in stability and transport. Importantly, implementations of the BKC are not limited to optomechanics; realizations can be envisioned in electronics, acoustics, photonics, and superconducting circuits. In a fully quantum setting, it would be interesting to study the behavior of fluctuations and the generation of many-body entanglement [50] — relevant to the use of the BKC and related phases in quantum sensing and information processing.

Acknowledgements

We acknowledge A. A. Clerk for discussions. M.B. acknowledges funding from the Swiss National Science Foundation (PCEFP2.194268). J.d.P. acknowledges financial support from the ETH Fellowship programme (grant no. 20-2 FEL-66). This work is part of the research programme of the Netherlands Organisation for Scientific Research (NWO). It is supported by the European Research Council (ERC starting grant no. 759644-TOPP).

[1] M. Z. Hasan and C. L. Kane, Colloquium: Topological insulators, *Rev. Mod. Phys.* **82**, 3045 (2010).
 [2] T. Ozawa, H. M. Price, A. Amo, N. Goldman, M. Hafezi, L. Lu, M. C. Rechtsman, D. Schuster, J. Simon, O. Zeitlinger, and I. Carusotto, Topological photonics, *Rev. Mod. Phys.* **91**, 015006 (2019).

[3] G. Ma, M. Xiao, and C. T. Chan, Topological phases in acoustic and mechanical systems, *Nat. Rev. Phys.* **1**, 281 (2019).
 [4] C. Nayak, S. H. Simon, A. Stern, M. Freedman, and S. Das Sarma, Non-abelian anyons and topological quantum computation, *Rev. Mod. Phys.* **80**, 1083 (2008).

- [5] C. Beenakker, Search for majorana fermions in superconductors, *Annu. Rev. Cond. Matt. Phys.* **4**, 113 (2013).
- [6] E. J. Bergholtz, J. C. Budich, and F. K. Kunst, Exceptional topology of non-Hermitian systems, *Rev. Mod. Phys.* **93**, 015005 (2021).
- [7] K. Ding, C. Fang, and G. Ma, Non-Hermitian topology and exceptional-point geometries, *Nat. Rev. Phys.* **4**, 745 (2022).
- [8] Z. Gong, Y. Ashida, K. Kawabata, K. Takasan, S. Higashikawa, and M. Ueda, Topological phases of non-Hermitian systems, *Phys. Rev. X* **8**, 031079 (2018).
- [9] K. Kawabata, S. Higashikawa, Z. Gong, Y. Ashida, and M. Ueda, Topological unification of time-reversal and particle-hole symmetries in non-Hermitian physics, *Nat. Commun.* **10**, 297 (2019).
- [10] K. Kawabata, K. Shiozaki, M. Ueda, and M. Sato, Symmetry and topology in non-Hermitian physics, *Phys. Rev. X* **9**, 041015 (2019).
- [11] V. Peano, M. Houde, F. Marquardt, and A. A. Clerk, Topological quantum fluctuations and traveling wave amplifiers, *Phys. Rev. X* **6**, 041026 (2016).
- [12] M. A. Bandres, S. Wittek, G. Harari, M. Parto, J. Ren, M. Segev, D. N. Christodoulides, and M. Khajavikhan, Topological insulator laser: Experiments, *Science* **359**, eaar4005 (2018).
- [13] J. C. Budich and E. J. Bergholtz, Non-Hermitian topological sensors, *Phys. Rev. Lett.* **125**, 180403 (2020).
- [14] S. Yao and Z. Wang, Edge states and topological invariants of non-Hermitian systems, *Phys. Rev. Lett.* **121**, 086803 (2018).
- [15] S. Yao, F. Song, and Z. Wang, Non-Hermitian Chern bands, *Phys. Rev. Lett.* **121**, 136802 (2018).
- [16] F. K. Kunst, E. Edvardsson, J. C. Budich, and E. J. Bergholtz, Biorthogonal bulk-boundary correspondence in non-Hermitian systems, *Phys. Rev. Lett.* **121**, 026808 (2018).
- [17] V. M. Martinez Alvarez, J. E. Barrios Vargas, and L. E. F. Foa Torres, Non-Hermitian robust edge states in one dimension: Anomalous localization and eigenspace condensation at exceptional points, *Phys. Rev. B* **97**, 121401 (2018).
- [18] N. Okuma, K. Kawabata, K. Shiozaki, and M. Sato, Topological origin of non-Hermitian skin effects, *Phys. Rev. Lett.* **124**, 086801 (2020).
- [19] K. Zhang, Z. Yang, and C. Fang, Correspondence between winding numbers and skin modes in non-Hermitian systems, *Phys. Rev. Lett.* **125**, 126402 (2020).
- [20] A. Ghatak, M. Brandenbourger, J. van Wezel, and C. Coullais, Observation of non-Hermitian topology and its bulk-edge correspondence in an active mechanical metamaterial, *Proc. Natl. Acad. Sci. U.S.A.* **117**, 29561 (2020).
- [21] T. Helbig, T. Hofmann, S. Imhof, M. Abdelghany, T. Kiessling, L. W. Molenkamp, C. H. Lee, A. Szameit, M. Greiter, and R. Thomale, Generalized bulk-boundary correspondence in non-Hermitian topoelectrical circuits, *Nat. Phys.* **16**, 747 (2020).
- [22] S. Weidemann, M. Kremer, T. Helbig, T. Hofmann, A. Stegmaier, M. Greiter, R. Thomale, and A. Szameit, Topological funneling of light, *Science* **368**, 311 (2020).
- [23] L. Xiao, T. Deng, K. Wang, G. Zhu, Z. Wang, W. Yi, and P. Xue, Non-Hermitian bulk-boundary correspondence in quantum dynamics, *Nat. Phys.* **16**, 761 (2020).
- [24] Q. Liang, D. Xie, Z. Dong, H. Li, H. Li, B. Gadway, W. Yi, and B. Yan, Dynamic signatures of non-Hermitian skin effect and topology in ultracold atoms, *Phys. Rev. Lett.* **129**, 070401 (2022).
- [25] L. Zhang, Y. Yang, Y. Ge, Y.-J. Guan, Q. Chen, Q. Yan, F. Chen, R. Xi, Y. Li, D. Jia, S.-Q. Yuan, H.-X. Sun, H. Chen, and B. Zhang, Acoustic non-Hermitian skin effect from twisted winding topology, *Nat. Commun.* **12**, 6297 (2021).
- [26] K. Wang, A. Dutt, K. Y. Yang, C. C. Wojcik, J. Vučković, and S. Fan, Generating arbitrary topological windings of a non-Hermitian band, *Science* **371**, 1240 (2021).
- [27] W. Wang, X. Wang, and G. Ma, Non-Hermitian morphing of topological modes, *Nature* **608**, 50 (2022).
- [28] A. McDonald, T. Pereg-Barnea, and A. A. Clerk, Phase-dependent chiral transport and effective non-Hermitian dynamics in a bosonic Kitaev-Majorana chain, *Phys. Rev. X* **8**, 041031 (2018).
- [29] A. Y. Kitaev, Unpaired Majorana fermions in quantum wires, *Phys.-Usp.* **44**, 131 (2001).
- [30] C.-W. Chen, N. Lera, R. Chaunsali, D. Torrent, J. V. Alvarez, J. Yang, P. San-Jose, and J. Christensen, Mechanical analogue of a Majorana bound state, *Adv. Mater.* **31**, 1904386 (2019).
- [31] K. Qian, D. J. Apigo, K. Padavić, K. H. Ahn, S. Vishveshwara, and C. Prodan, Observation of Majorana-like bound states in metamaterial-based Kitaev chain analogs, *Phys. Rev. Res.* **5**, L012012 (2023).
- [32] C. C. Wanjura, M. Brunelli, and A. Nunnenkamp, Topological framework for directional amplification in driven-dissipative cavity arrays, *Nat. Commun.* **11**, 3149 (2020).
- [33] A. McDonald and A. A. Clerk, Exponentially-enhanced quantum sensing with non-Hermitian lattice dynamics, *Nat. Commun.* **11**, 5382 (2020).
- [34] V. P. Flynn, E. Cobanera, and L. Viola, Topology by dissipation: Majorana bosons in metastable quadratic markovian dynamics, *Phys. Rev. Lett.* **127**, 245701 (2021).
- [35] J. P. Mathew, J. del Pino, and E. Verhagen, Synthetic gauge fields for phonon transport in a nano-optomechanical system, *Nat. Nanotechnol.* **15**, 198 (2018).
- [36] J. del Pino, J. J. Slim, and E. Verhagen, Non-Hermitian chiral phononics through optomechanically-induced squeezing, *Nature* **606**, 82 (2021).
- [37] See supplementary information.
- [38] C. C. Wanjura, J. J. Slim, J. del Pino, M. Brunelli, E. Verhagen, and A. Nunnenkamp, Quadrature nonreciprocity in bosonic networks without breaking time-reversal symmetry, *Nat. Phys.* [10.1038/s41567-023-02128-x](https://doi.org/10.1038/s41567-023-02128-x) (2023).
- [39] A. Metelmann and A. A. Clerk, Nonreciprocal photon transmission and amplification via reservoir engineering, *Phys. Rev. X* **5**, 021025 (2015).
- [40] N. Hatano and D. R. Nelson, Vortex pinning and non-Hermitian quantum mechanics, *Phys. Rev. B* **56**, 8651 (1997).
- [41] Y. Xiong, Why does bulk boundary correspondence fail in some non-hermitian topological models, *J. Phys. Commun.* **2**, 035043 (2018).
- [42] C. Coullais, R. Fleury, and J. van Wezel, Topology and broken Hermiticity, *Nat. Phys.* **17**, 9 (2021).

- [43] M. Brunelli, C. C. Wanjura, and A. Nunnenkamp, Restoration of the non-Hermitian bulk-boundary correspondence via topological amplification. [arXiv:2207.12427](https://arxiv.org/abs/2207.12427) [quant-ph], (2022).
- [44] D. Porras and S. Fernández-Lorenzo, Topological amplification in photonic lattices, *Phys. Rev. Lett.* **122**, 143901 (2019).
- [45] C. C. Wanjura, M. Brunelli, and A. Nunnenkamp, Correspondence between non-Hermitian topology and directional amplification in the presence of disorder, *Phys. Rev. Lett.* **127**, 213601 (2021).
- [46] L.-L. Wan and X.-Y. Lü, Quantum-squeezing-induced point-gap topology and skin effect, *Phys. Rev. Lett.* **130**, 203605 (2023).
- [47] C. E. Bardyn and A. Imamoglu, Majorana-like modes of light in a one-dimensional array of nonlinear cavities, *Phys. Rev. Lett.* **109**, 1 (2012).
- [48] Y. Barlas and E. Prodan, Topological braiding of non-abelian midgap defects in classical metamaterials, *Phys. Rev. Lett.* **124**, 146801 (2020).
- [49] Y. S. S. Patil, J. Höller, P. A. Henry, C. Guria, Y. Zhang, L. Jiang, N. Kralj, N. Read, and J. G. E. Harris, Measuring the knot of non-Hermitian degeneracies and non-commuting braids, *Nature* **607**, 271–275 (2022).
- [50] G. Lee, T. Jin, Y.-X. Wang, A. McDonald, and A. Clerk, Entanglement phase transition due to reciprocity breaking without measurement or post-selection. [arXiv:2308.14614](https://arxiv.org/abs/2308.14614) [quant-ph], (2023).

Supplementary Information

I. SUPPLEMENTARY EXPERIMENTAL DETAILS: CONTROLLING THE BKC INTERACTION HAMILTONIAN AND MEASUREMENT OF QUADRATURE-RESOLVED SUSCEPTIBILITY

We use the techniques outlined in [1–3] to synthesize arbitrary quadratic bosonic Hamiltonians in a network of nanomechanical modes controlled through temporally modulated radiation pressure of control lasers. In the following, we briefly outline the main working principles and methods that we use to implement the Hamiltonian and read out the response of the system.

A. Experimental system

The nano-optomechanical device used in this study comprises a suspended silicon sliced nanobeam featuring a photonic crystal cavity (optical mode frequency $\omega_c/(2\pi) = 195.451$ THz, linewidth $\kappa/(2\pi) = 320$ GHz) coupled to multiple non-degenerate, flexural mechanical modes. Details on design, fabrication, and characterization of the device can be found in [2, 3]. We use the lowest five mechanical modes (‘resonators’) of the set of strings that compose the nanobeam, with spatial profiles as shown in Fig. 1a of the main text and frequencies $\omega_j/(2\pi) = \{3.7, 5.3, 12.8, 17.6, 26.3\}$ MHz, to construct the chains studied in this work. These mechanical resonators have intrinsic linewidths $\gamma_j/(2\pi) \approx 1\text{--}7$ kHz and couple dispersively to the optical cavity mode with vacuum optomechanical coupling $g_{0,j}/(2\pi) \approx \{5.3, 5.9, 3.3, 3.1, 1.9\}$ MHz. These are defined as the cavity frequency shift induced by a mechanical displacement of the respective mode equal to the magnitude of its ground state fluctuations [4]. Light is coupled in and out of the cavity from free space, by focusing a laser beam at normal incidence to the sample surface, in a cross-polarized detection scheme. The coupling efficiency is approximately 3%, and typical incident laser powers are of the order of milliwatts. The sample is positioned in a vacuum chamber (pressure 2×10^{-6} mbar), and aligned to the laser focus using a piezo-actuated precision stage.

B. Parametric control

Direct mechanical interaction between the non-degenerate flexural modes is prevented by their large frequency spacing and narrow linewidths. Nevertheless, suitable modulation of radiation pressure backaction can enable controllable, light-mediated effective mechanical interactions [2, 3, 5].

In the unresolved sideband regime or bad-cavity limit, where $\omega_j \ll \kappa$ as in our system, the cavity photon population n_c responds to optical driving instantaneously on mechanical timescales. Moreover, with the control laser (Toptica CTL 1500) optimally tuned to the flank of the resonance $\Delta = \kappa/(2\sqrt{3})$, the dispersive coupling of mechanical displacement to the cavity frequency induces maximal modulations of n_c . Here, $\Delta = \omega_l - \omega_c$ denotes the detuning of the laser with frequency ω_l from the cavity resonance frequency. For a single resonator, the resulting mechanically modulated radiation pressure force acts back on the resonator’s displacement, giving rise to the well-known optical spring effect [4], where the resonator experiences a shift $\delta\omega_j = 2g_j^2\Delta/(\Delta^2 + \kappa^2/4)$ in its frequency. Here $g_j = \sqrt{\bar{n}_c}g_{0,j}$ is the optomechanical coupling enhanced by the average cavity population \bar{n}_c .

In our multimode system, the displacement of each resonator contributes a modulation to n_c . The ensuing modulated radiation pressure forces in principle generate ‘cross-resonator’ optical springs, where the displacement of one resonator induces a force on the other ones [6]. For fixed drive laser intensity and non-degenerate modes, those forces cause off-resonant drives and do not induce appreciable interaction between the resonators. However, by temporally modulating the laser drive we can parametrically couple the modes, using cross-resonator optical springs to induce resonant interactions between mechanical modes. In particular, a harmonic modulation of the drive laser intensity with frequency ω_m set to the frequency difference $\omega_m = \omega_k - \omega_j$ (frequency sum $\omega_m = \omega_k + \omega_j$) of two modes j, k stimulates a frequency conversion process and induces an effective mechanical beamsplitter (squeezing) interaction after adiabatic elimination of the cavity field [1, 2]. The depth c_m of the harmonic modulation tone controls the effective interaction strength $|J_{jk}|$ ($|\lambda_{jk}|$) as

$$|J_{jk}|, |\lambda_{jk}| = c_m \frac{g_j g_k \Delta}{\Delta^2 + \kappa^2/4} = c_m \frac{\sqrt{\delta\omega_j \delta\omega_k}}{2}, \quad (\text{S1})$$

while the phase offset ϕ_m of the modulation sets the interaction phase in the appropriate rotating frame as $J_{jk} \equiv |J_{jk}|e^{i\phi_m}$ or $\lambda_{jk} \equiv |\lambda_{jk}|e^{i\phi_m}$. This is crucial for controlling the coupling phase φ discussed in the main text, and in

particular, to generate the required imaginary couplings to construct the bosonic Kitaev chain (BKC) shown in Figs. 1 and 2.

We note that while accurately estimating $g_j = \sqrt{n_c}g_{0,j}$ can be challenging, the individual resonator spring shifts $\delta\omega_j$ are readily measured. Finally, modulation tones can be superimposed to induce multiple interactions, as all our mechanical frequencies are incommensurate. The required modulation tones are generated by a high-frequency lock-in amplifier (Zurich Instruments UHFLL) as well several additional signal generators (Siglent SDG1062X and SDG2122X) whose clocks are synchronized with that of the lock-in amplifier (section IE). The signals are amplified and sent to fiber-coupled intensity modulators (Thorlabs LN81S-FC and Covega Mach-10 056) to modulate the control laser intensity.

C. BKC Hamiltonian and dynamics

The BKC Hamiltonian [7] that we implement combines beam-splitter and two-mode squeezing interactions between neighboring modes that are uniform along the chain, i.e. $J_{jk} = J, \lambda_{jk} = \lambda$. It reads (see equation (1) in the main text)

$$H_{\text{BKC}} = \sum_j \left(J a_{j+1}^\dagger a_j + \lambda a_{j+1}^\dagger a_j^\dagger + \text{H.c.} \right), \quad (\text{S2})$$

where mechanical modes are described by their field operators a_j in a frame rotating along with the resonators. For most of the main text, we focus on the case $J = i|J|$ and $\lambda = i|\lambda|$, in which case the Hamiltonian expressed in terms of the field quadratures $x_j \equiv (a_j + a_j^\dagger)/\sqrt{2}$, $p_j \equiv -i(a_j - a_j^\dagger)/\sqrt{2}$ simplifies to [7]

$$H_{\text{BKC}} = \sum_j (|\lambda| - |J|)x_{j+1}p_j + (|\lambda| + |J|)p_{j+1}x_j. \quad (\text{S3})$$

The field quadratures evolving according to the Hamiltonian (S3) obey Heisenberg-Langevin equations of motion

$$\dot{x}_j = -\frac{\gamma_j}{2}x_j + (|J| + |\lambda|x_{j-1} - (|J| - |\lambda|x_{j+1} - \sqrt{\gamma_j}x_{j,\text{in}} \quad (\text{S4})$$

$$\dot{p}_j = -\frac{\gamma_j}{2}p_j + (|J| - |\lambda|)p_{j-1} - (|J| + |\lambda|)p_{j+1} - \sqrt{\gamma_j}p_{j,\text{in}}. \quad (\text{S5})$$

Here, $x_{j,\text{in}}$ and $p_{j,\text{in}}$ denote external driving quadratures, which quantify the probing forces that act on the resonators.

Equations (S4) and (S5) define the dynamical matrix \mathcal{M}

$$\begin{aligned} \begin{pmatrix} \dot{\mathbf{x}} \\ \dot{\mathbf{p}} \end{pmatrix} &= \begin{pmatrix} -\frac{\Gamma}{2} + \mathcal{H} & 0 \\ 0 & -\frac{\Gamma}{2} - \mathcal{H}^\text{T} \end{pmatrix} \begin{pmatrix} \mathbf{x} \\ \mathbf{p} \end{pmatrix} - \sqrt{\Gamma} \begin{pmatrix} \mathbf{x}_{\text{in}} \\ \mathbf{p}_{\text{in}} \end{pmatrix} \\ &= \mathcal{M} \begin{pmatrix} \mathbf{x} \\ \mathbf{p} \end{pmatrix} - \sqrt{\Gamma} \begin{pmatrix} \mathbf{x}_{\text{in}} \\ \mathbf{p}_{\text{in}} \end{pmatrix} \end{aligned} \quad (\text{S6})$$

with $\Gamma = \text{diag}(\gamma_1, \dots, \gamma_N)$ and in which we collected the quadratures in the vectors $\mathbf{x} \equiv (x_1, \dots, x_N)^\text{T}$ and $\mathbf{p} \equiv (p_1, \dots, p_N)^\text{T}$, and similarly for \mathbf{x}_{in} and \mathbf{p}_{in} .

We note the symmetry of the dynamical matrix which relates the dynamical matrices $M_x \equiv -\frac{\Gamma}{2} + \mathcal{H}$ and $M_p \equiv -\frac{\Gamma}{2} - \mathcal{H}^\text{T}$ for the x and p quadratures, respectively. For both open and periodic boundary conditions, the matrix \mathcal{H} is defined as $\mathcal{H}_{j,j+1} = |\lambda| - |J|$ and $\mathcal{H}_{j+1,j} = |\lambda| + |J|$, i.e., the effective coupling strengths to the left and to the right are asymmetric, $\mathcal{H}_{j,j+1} \neq \mathcal{H}_{j+1,j}$, so that the dynamic matrix \mathcal{M} realises two copies of the Hatano-Nelson model. For periodic boundary conditions, additionally, $\mathcal{H}_{N,1} = |\lambda| - |J|$ and $\mathcal{H}_{1,N} = |\lambda| + |J|$.

The susceptibility matrix encodes the steady-state system response to the quadratures of the external probe field at frequency ω and is calculated from the dynamical matrix \mathcal{M} according to

$$\chi(\omega) = (i\omega\mathbf{1} + \mathcal{M})^{-1}. \quad (\text{S7})$$

As such, $\chi(\omega)$ describes the linear response of the quadratures $(\mathbf{x}, \mathbf{p})^\text{T}$ to a ‘drive’ defined as $\mathbf{f}^{(\mathbf{q})} = \sqrt{\Gamma}(\mathbf{x}_{\text{in}}, \mathbf{p}_{\text{in}})^\text{T}$ with frequency ω .

As we concern ourselves only with the mechanical response at resonance in this study, we introduce the short-hand $\chi \equiv \chi(0)$. In the main text, we refer to \mathcal{M} also as the ‘non-Hermitian Hamiltonian matrix’, which is thus the inverse of the resonant susceptibility $\chi = \mathcal{M}^{-1}$. We assume equal decay rates $\gamma_j = \gamma$ for all the mechanical modes, which

the phase difference

$$\begin{aligned}\Delta\phi_m^{(j\pm k)} &= \beta_{j\pm k}(t) - (\beta_j(t) \pm \beta_k(t)) \\ &= \phi_m^{(j\pm k)} - \left(\phi_m^{(j)} \pm \phi_m^{(k)}\right)\end{aligned}\tag{S10}$$

is stable and does not depend on the origin of time. Physically, this phase difference may be evaluated by generating a tone with the combined instantaneous phase $\beta_j(t) \pm \beta_k(t)$ through mixing of the LOs and subsequent high-pass (low-pass) filtering, and comparing that to the interaction tone.

As we work with relatively low modulation frequencies in the MHz range, we can take a digital approach to achieve phase coherence. In fact, the lock-in amplifier we use is a digital device based on 8 numerical oscillators operating at a clock frequency of 1.8 GHz, and synthesizes its output tones on-the-fly. We can therefore access the instantaneous phase $\beta_l(t)$ directly. Note that the actual output signal lags the numerical oscillator by a time delay that depends on the oscillator index, equal to 16 clock cycles per oscillator.

If only the LIA is used to generate control tones and no external signal generators are involved, we execute the following procedure. Before starting an experiment, at time t_0 , we simultaneously access the instantaneous phases $\beta_l(t_0)$ of all numerical oscillators, generating LO and interaction tones alike. We then apply a phase shift equal to $-\beta_l(t_0)$ to all oscillators, effectively defining t_0 as the origin of time. Finally, we shift the interaction tone oscillators to generate the desired interaction phases $\arg(J_{jk}), \arg(\lambda_{jk})$ in the rotating frame.

If an experiment requires more LOs and control signals than the 8 numerical oscillators of the LIA can provide, we follow an extension of this procedure that is conceptually similar but involves a more elaborate phase bookkeeping. Suppose we want to monitor the dynamics of N mechanical resonators under the influence of M modulation tones, with $N + M > 8$. As we require the LIA to analyse the mechanical signal, we implement up to $N = 7$ resonator LOs using the lowest-index numerical oscillators. The remaining free LIA oscillators are used to generate the first $8 - N$ interaction tones. The $M + N - 8$ interaction tones that remain need to be generated by external signal generators.

During the phase referencing procedure, we temporarily use the LIA oscillator with highest index $m = 8$ to ‘transfer’ phase coherence between the LIA and the external signal sources. First, we achieve phase coherence between the oscillators internal to the LIA as described earlier. For each externally generated modulation tone $l = j \pm k$, we execute the following steps:

1. Set the frequency of LIA oscillator $m = 8$ to match the frequency $\omega_m^{(l)} = \omega_j \pm \omega_k$ of the external signal generator.
2. Access the instantaneous phases $\beta_8(t)$ of the phase transfer oscillator 8 and $\beta_j(t), \beta_k(t)$ of the relevant resonator LOs.
3. Use (S10) to evaluate the current, *arbitrary* phase $\Delta\phi_m^{(l)}$ of oscillator 8 in the rotating frame.
4. Shift the phase of oscillator 8 by $-\Delta\phi_m^{(l)}$ to cancel its current phase offset. We have now achieved phase coherence between the tone generated by the phase transfer oscillator and the resonator LOs.
5. Set the LIA to output a small voltage at $\omega_m^{(l)}$ using oscillator 8. This signal imprints a weak modulation on the control laser that we detect by tapping off part of the control laser light and feeding that onto a separate ‘monitor’ detector.
6. Analyse the monitor signal using the same LIA oscillator 8 to evaluate the phase α_1 of the imprinted modulation, combined with signal delay through part of the set-up.
7. Disable the LIA output and enable a small output voltage at $\omega_m^{(l)}$ on the external signal generator.
8. Measure the phase α_2 of the imprinted modulation using LIA oscillator 8.
9. Shift the phase of the external signal source by $-(\alpha_2 - \alpha_1)$ to achieve phase coherence between the LIA-generated tone and the externally generated tone.
10. Shift the phase of the external signal source to generate the desired interaction phase $\arg(J_{jk}), \arg(\lambda_{jk})$ in the rotating frame. We are now done, and move on to the next external tone.

As a final step, the phase coherence of the interaction tone originally assigned to oscillator 8 is restored by following the procedure above up to step 4.

F. Dissipation control

We implement measurement-based feedback to equalize the decay rates of the individual resonators to $\gamma_j = \gamma$, by applying a radiation pressure force proportional to each resonator’s velocity. To do so, we modulate the weak drive laser with real-time feedback signals generated from the electronic displacement record by a digital signal processor (DSP, RedPitaya STEMLab 125-14) that implements a configurable bandpass filter for each resonator. Each filter’s phase shift is tuned to provide velocity feedback to its respective resonator while the gain is varied to attain the desired damping rate. Details on calibration procedures can be found in [2].

II. SUPPLEMENTARY THEORETICAL DETAILS: SPECTRAL WINDING AND SYMMETRY

A. Spectral winding in the BKC

As shown in Ref. [8], the BKC displays non-trivial non-Hermitian phases corresponding to directional amplification which occurs in opposite directions for the x and the p quadratures in which the respective end-to-end gain grows exponentially with the chain length N .

In the special case, $\varphi = \frac{\pi}{2}$, the situation is particularly simple. The equations for x and p decouple and we can consider the x and p chain separately. In particular, in the plane wave basis $x_k \equiv \frac{1}{\sqrt{N}} \sum_j e^{ikj} x_j$ and $p_k \equiv \frac{1}{\sqrt{N}} \sum_j e^{-ikj} p_j$, the dynamical matrix $\mathcal{M}_{xp}(k)$ governing the evolution of $\mathbf{q}_k = (x_k, p_k)^T$ according to $\dot{\mathbf{q}}_k = \mathcal{M}_{xp}(k)\mathbf{q}_k - \sqrt{\gamma}\mathbf{q}_{k,\text{in}}$ is already diagonal

$$\mathcal{M}_{xp}(k) = \begin{pmatrix} \omega_x(k) & 0 \\ 0 & \omega_p(k) \end{pmatrix}, \quad (\text{S11})$$

with the spectrum $\omega_{x,p}(k) = -i\frac{\gamma}{2} - 2J \sin k \mp 2i\lambda \cos k$ given in Eq. (3) of the main text.

Accordingly, we define the winding numbers $\nu_{x,p}$ on the spectrum for periodic boundary conditions (PBC) (S11) $\omega_{x,p}(k)$ as given in Eq. (3) of the main text through [8]

$$\nu_{x,p} \equiv \frac{1}{2\pi i} \int_0^{2\pi} dk \frac{\partial \omega_{x,p}(k)/\partial k}{\omega_{x,p}(k)}, \quad (\text{S12})$$

which are $\nu_x = -1$ and $\nu_p = +1$ for $2|\lambda| > \gamma/2$ and $\nu_x = \nu_p = 0$ otherwise.

The Hamiltonian of the generalized BKC is given by

$$H_{\text{BKC}} = \sum_j \left[|J| e^{i\varphi} a_{j+1}^\dagger a_j + |\lambda| e^{i\varphi} a_{j+1}^\dagger a_j^\dagger + \text{H.c.} \right]. \quad (\text{S13})$$

In general, this Hamiltonian leads to coupled equations of motion for x and p , so the formula above, Eq. (S12), cannot be applied directly to compute the winding numbers. Instead, we will diagonalise the Bloch dynamical matrix under periodic boundary conditions to find a transformed set of quadratures for which the dynamical equations decouple.

To study the system under periodic boundary conditions, we introduce $a_k \equiv \frac{1}{\sqrt{N}} \sum_j e^{ikj} a_j$, $a_k^\dagger \equiv \frac{1}{\sqrt{N}} \sum_j e^{-ikj} a_j^\dagger$ and $a_{-k} \equiv \frac{1}{\sqrt{N}} \sum_j e^{-ikj} a_j$, $a_{-k}^\dagger \equiv \frac{1}{\sqrt{N}} \sum_j e^{ikj} a_j^\dagger$. This yields

$$H_{\text{BKC}}^{\text{PBC}} = \sum_j \left[2|J| \cos(k + \varphi) a_k^\dagger a_k + |\lambda| (e^{ik} e^{i\varphi} a_k^\dagger a_{-k}^\dagger + e^{-ik} e^{-i\varphi} a_k a_{-k}) \right]. \quad (\text{S14})$$

This allows us to compute the dynamical matrix under periodic boundary conditions for the vector $\alpha_k^T = (a_k, a_{-k}^\dagger)^T$ with $k \in [0, 2\pi)$ satisfying $\dot{\alpha}_k = \mathcal{M}_\alpha \alpha_k - \sqrt{\gamma} \alpha_{k,\text{in}}$ with

$$\mathcal{M}_\alpha(k) = \begin{pmatrix} -i\frac{\gamma}{2} + 2|J| \cos(k + \varphi) & 2e^{i\varphi} |\lambda| \cos k \\ -2e^{-i\varphi} |\lambda| \cos k & -i\frac{\gamma}{2} - 2|J| \cos(-k + \varphi) \end{pmatrix}. \quad (\text{S15})$$

The eigenvalues of this matrix are given by

$$\omega_\pm(k) = -i\frac{\gamma}{2} - \left(2|J| \sin \varphi \sin k \pm 2i\sqrt{|\lambda|^2 - |J|^2 \cos^2 \varphi} \cos k \right). \quad (\text{S16})$$

At $\varphi = \frac{\pi}{2}$, we recover $\omega_+(k) = \omega_x(k)$ and $\omega_-(k) = \omega_p(k)$ of Eq. (3) in the main text. As we show below, importantly, the corresponding eigenvectors are independent of k , which implies that there exists a local transformation that maps back to the BKC at $\varphi = \frac{\pi}{2}$ [7]. As a consequence the correspondence between non-trivial, non-Hermitian topology and directional end-to-end amplification [8] applies to the BKC for all φ . If the transformation was not local, there could, in principle, still be a basis in which the system displays directional amplification, but the amplification does not have to be end-to-end or even directional in real space. Since here the transformation is local, it is justified to study the winding of $\omega_\pm(k)$ which can then again be related to directional end-to-end amplification under open

boundary conditions. Analogously, the winding numbers ν_{\pm} of $\omega_{\pm}(k)$ are defined according to

$$\nu_{\pm} \equiv \frac{1}{2\pi i} \int_0^{2\pi} dk \frac{\partial \omega_{\pm}(k)/\partial k}{\omega_{\pm}(k)}. \quad (\text{S17})$$

We notice from the expression for the spectrum (S16) there are two cases: either $|(J/\lambda) \cos \varphi| < 1$ or $|(J/\lambda) \cos \varphi| > 1$. In the first case, the term under the square root in Eq. (S16) is positive, so $\omega_{\pm}(k)$ is complex and the point gap is open (see Fig. 3 in the main text). The winding number (S17) can be +1, -1 or 0. In the second case, the term under the square root is negative, so the k -dependent terms of the spectrum are all real and the point gap is closed (see Fig. 3 in the main text). The winding number (S17) is always zero.

Next, we show explicitly that the eigenvectors are independent of k . Introducing, $y \equiv |J/\lambda| \cos \varphi$, we can express the corresponding eigenvectors as

$$\begin{aligned} |\Psi_+\rangle &\equiv \frac{1}{\mathcal{N}_+} (e^{i\varphi}[-y + \sqrt{y^2 - 1}], 1)^T, \\ |\Psi_-\rangle &\equiv \frac{1}{\mathcal{N}_-} (e^{i\varphi}[-y - \sqrt{y^2 - 1}], 1)^T, \end{aligned} \quad (\text{S18})$$

with the normalization constant

$$\mathcal{N}_{\pm} \equiv \begin{cases} \sqrt{1 + (y \pm \sqrt{y^2 - 1})^2} & : |y| \geq 1 \\ \sqrt{2} & : |y| < 1 \end{cases}. \quad (\text{S19})$$

The eigenvectors also differ in the two cases mentioned above. In the first case $|(J/\lambda) \cos \varphi| < 1$ (point gap open), defining $y \equiv |J/\lambda| \cos \varphi = \cos \eta$ simplifies the eigenvectors to

$$|\Psi_+\rangle \equiv \frac{1}{\sqrt{2}} (-e^{i(\varphi-\eta)}, 1)^T, \quad |\Psi_-\rangle \equiv \frac{1}{\sqrt{2}} (-e^{i(\varphi+\eta)}, 1)^T. \quad (\text{S20})$$

In the second case $|(J/\lambda) \cos \varphi| > 1$ (point gap closed), defining $\cosh \xi \equiv y$ leads to the eigenvectors

$$|\Psi_+\rangle \equiv \frac{1}{\sqrt{1 + e^{-2|\xi|}}} (-e^{-|\xi|}, 1)^T, \quad |\Psi_-\rangle \equiv \frac{1}{\sqrt{1 + e^{2|\xi|}}} (-e^{|\xi|}, 1)^T. \quad (\text{S21})$$

B. Parity symmetry of the BKC

We mentioned in the main text that the BKC preserves parity symmetry [9] for any phase φ . Intuitively, parity symmetry implies that reflecting the system and performing a suitable *local* transformation, the system remains unchanged. In the BKC at $\varphi = \frac{\pi}{2}$ this is particularly easy to see since reflecting the system and swapping x and p we obtain the same response (see the susceptibility matrices in Fig. 1). This can be generalized to arbitrary φ . In particular, we notice that the eigenvalues in Eq. (S16) satisfy

$$\omega_+ \left(k + \frac{\pi}{2} \right) = \omega_- \left(-k + \frac{\pi}{2} \right). \quad (\text{S22})$$

This leads to a condition for $\mathcal{M}_{\alpha}(k)$

$$\mathcal{M}_{\alpha} \left(k + \frac{\pi}{2} \right) V = V \mathcal{M}_{\alpha} \left(-k + \frac{\pi}{2} \right), \quad (\text{S23})$$

with $V = (|\Psi_+\rangle, |\Psi_-\rangle)$. Eq. (S23) is the formal definition of parity symmetry [9]. Note that as a consequence of parity symmetry, the two winding numbers ν_{\pm} , Eq. (S17), associated with $\omega_{\pm}(k)$ have opposite sign. Since the eigenvectors (S18) are independent of k , the transformation V is local. Alternatively, we can take a different view point: as long as Eq. (S23) holds and V is local (k independent), we can compute the winding numbers of $\omega_{\pm}(k)$ and we can relate this winding number to directional amplification under open boundary conditions. In that sense, parity symmetry *protects* non-Hermitian topology and the associated scattering properties.

This symmetry is broken in the presence of detuning since in that case the eigenvectors become k dependent and the transformation V is no longer local.

III. THERMAL STEADY-STATES

In the absence of coherent driving, the BKC is subject to thermal forces. Squeezing in the chain then provides amplification of the resulting thermal fluctuations above their equilibrium level in the absence of interactions, as shown in Fig. 2.

For a BKC with four sites coupled to individual thermal baths with occupancies $n_{j,\text{th}}$, we calculate the average phonon populations n_j^{OBC} and n_j^{PBC} under open and closed boundary conditions, respectively. For simplicity, we assume $n_{j,\text{th}} = n_{\text{th}}$, which holds to reasonable approximation in our experiment due the provided feedback cooling. Using the quantum regression theorem [2, 10], the populations of the first resonator are then given by

$$n_1^{\text{OBC}} = n_{\text{th}} \left(1 + G^2/4 + 3G^4/16 + 5G^6/32 \right), \quad (\text{S24})$$

$$n_1^{\text{PBC}} = n_{\text{th}} \left(1 + \frac{1}{2} \frac{G^2}{1 - G^2} \right). \quad (\text{S25})$$

These expressions define the theory lines in Fig. 2b. While equation (S24) remains finite for any value of G , the dynamical instability under periodic boundary conditions is signified by the fact that n_1^{PBC} tends to infinity for $G \rightarrow 1$ in equation (S25).

Since the closed chain with equal bath occupations is translationally invariant, expression (S25) holds in fact for all resonators. This does not apply to the open chain, where we find that the two outer sites $n_1^{\text{OBC}} = n_4^{\text{OBC}}$ have equal populations, whereas the inner sites have

$$n_2^{\text{OBC}} = n_3^{\text{OBC}} = n_{\text{th}} \left(1 + G^2/2 + 3G^4/16 \right), \quad (\text{S26})$$

that grow as a polynomial in G with lower degree than in (S25). This reflects the shorter length of the effective amplification chains that feed the inner sites.

IV. EXPONENTIALLY ENHANCED RESPONSIVITY FOR NON-TRIVIAL NON-HERMITIAN TOPOLOGY

Here, we show that the exponential increase in responsivity reported in the main text is a signature of non-trivial, non-Hermitian topology. An exponential sensitivity to boundary conditions in non-Hermitian systems with a point gap was remarked on in Ref. [11] and explored for sensing applications in Ref. [12]. The setup proposed by McDonald et al. [13] which we explore here is instead based on the exponential amplification of the unperturbed system under open boundary conditions and has the advantage that the system cannot become dynamically unstable for some values of the quantity that is to be sensed. Here, we identify the origin of the complex plane as a relevant reference point and rigorously prove that non-trivial values of a winding number calculated w.r.t. the origin (under PBC) are in one-to-one correspondence with the exponential scaling of the sensitivity with system size (under OBC).

In the sensing setup considered in the main text, we consider the BKC (S2) at $\varphi = \pi/2$ and couple the N th site of the chain to a system which we would like to sense and we assume that we introduce a detuning on the last site. Without this detuning, the equations of motion can be written in the block form of \mathcal{M} in Eq. (S6). In this configuration, the x chain is amplified from 1 to N and the p chain in the opposite direction [13].

The introduction of the detuning ε on the last site couples the x and p quadratures on that site

$$\dot{x}_N = -\varepsilon p_N + \left(-\frac{\Gamma}{2} \mathbf{x} + \mathcal{H} \mathbf{x} \right)_N - \sqrt{\gamma} x_{N,\text{in}}, \quad (\text{S27})$$

$$\dot{p}_N = \varepsilon x_N + \left(-\frac{\Gamma}{2} \mathbf{p} - \mathcal{H}^T \mathbf{p} \right)_N - \sqrt{\gamma} p_{N,\text{in}}. \quad (\text{S28})$$

This coupling allows for a signal in the x quadrature to be amplified along the x chain from site 1 to site N with a gain that is exponential in the chain length, converted to a signal in p depending on the strength of the detuning ε , and amplified back to site 1 with exponentially large gain [13].

We showed in Ref. [8] that the gain is exponential in system size if and only if the system's non-Hermitian topology is non-trivial. As the conversion from x to p quadrature depends on the strength of the detuning at the N th site, it is plausible that the sensitivity with which we can sense the change in detuning scales exponentially with system size.

We now proceed to make this argument more rigorous. Adopting the Dirac notation for matrix elements, we can

write the dynamical matrix $\mathcal{M}^{(\varepsilon)}$ of the system that includes the detuning at the last site

$$\mathcal{M}^{(\varepsilon)} = \begin{pmatrix} -\frac{\Gamma}{2} + \mathcal{H} & -\varepsilon |N\rangle\langle N| \\ \varepsilon |N\rangle\langle N| & -\frac{\Gamma}{2} - \mathcal{H}^T \end{pmatrix}. \quad (\text{S29})$$

We now derive an analytic formula for the susceptibility matrix $\chi^{(\varepsilon)} = (i\omega\mathbb{1} + \mathcal{M}^{(\varepsilon)})^{-1}$ and relate it to the susceptibility matrix without detuning $\chi(\omega)$

$$\chi(\omega) = \begin{pmatrix} (i\omega\mathbb{1} - \frac{\Gamma}{2} + \mathcal{H})^{-1} & 0 \\ 0 & (i\omega\mathbb{1} - \frac{\Gamma}{2} - \mathcal{H}^T)^{-1} \end{pmatrix} = \begin{pmatrix} \chi_{xx}(\omega) & 0 \\ 0 & \chi_{pp}(\omega) \end{pmatrix}. \quad (\text{S30})$$

To that purpose, we employ a formula for the inverse [14] of a sum of a matrix A and a rank-one matrix E and apply it recursively—a technique that was also used in [8] to derive the one-to-one correspondence between non-trivial, non-Hermitian topology and directional amplification. Concretely, $(A + E_j)^{-1} = A^{-1} - \frac{1}{1+g_j} A^{-1} E_j A^{-1}$ with $g_j \equiv \text{tr}(A^{-1} E_j)$ [15].

Here, we need to calculate $\chi^{(\varepsilon)}(\omega) = (i\omega\mathbb{1} + \mathcal{M} + \varepsilon[|N, p\rangle\langle N, x| - |N, x\rangle\langle N, p|])^{-1}$. Both $|N, p\rangle\langle N, x|$ and $|N, x\rangle\langle N, p|$ are rank-one, so we can apply the formula above recursively. This gives rise to the following expression for $\chi^{(\varepsilon)}(\omega)$

$$\chi^{(\varepsilon)}(\omega) = \chi + \frac{\varepsilon}{1 + \varepsilon^2 (\chi_{x_N \rightarrow x_N})^2} (\chi |p, N\rangle\langle x, N| \chi - \chi |x, N\rangle\langle p, N| \chi) + \varepsilon (\chi |x, N\rangle\langle x, N| \chi - \chi |p, N\rangle\langle p, N| \chi). \quad (\text{S31})$$

For clarity, we omitted the argument ω on the right-hand-side of Eq. (S31). We obtain the optimal sensitivity to changes in ε by measuring the response at the first site, i.e.,

$$\chi_{p_1 \rightarrow x_1}^{(\varepsilon)} = -\chi_{x_1 \rightarrow p_1}^{(\varepsilon)} = \frac{\varepsilon}{1 + \varepsilon^2 (\chi_{x_N \rightarrow x_N})^2} (\chi_{x_1 \rightarrow x_N})^2 \quad (\text{S32})$$

in which $\chi_{x_1 \rightarrow x_N} \propto e^{\alpha N}$ with $\alpha > 1$ in topologically non-trivial phases. Eq. (S32) is exact for the BKC at $|J| = |\lambda|$ and $\varphi = \pi/2$ which constitutes the exceptional point at which the reverse transmission is exactly zero leading to the cancellation of contributions from the third term in Eq. (S31) to $\chi_{p_1 \rightarrow x_1}^{(\varepsilon)}$. Otherwise, Eq. (S32) is exact up to an exponentially small correction of the order $e^{-\alpha N}$ with $\alpha > 1$.

Close to $\varepsilon = 0$, $\chi_{p_1 \rightarrow x_1}^{(\varepsilon)}$ is linear in ε with a slope that grows exponentially in system size. This is straightforward to see from Eq. (S32)

$$\frac{\partial \chi_{p_1 \rightarrow x_1}^{(\varepsilon)}}{\partial \varepsilon} = -\frac{\partial \chi_{x_1 \rightarrow p_1}^{(\varepsilon)}}{\partial \varepsilon} = \frac{1 - \varepsilon^2 (\chi_{x_N \rightarrow x_N})^2}{[1 + \varepsilon^2 (\chi_{x_N \rightarrow x_N})^2]^2} (\chi_{x_1 \rightarrow x_N})^2. \quad (\text{S33})$$

Around $\varepsilon = 0$, we define the linear responsivity as given in Eq. (4) of the main text

$$\mathcal{R} \equiv \gamma \left| \frac{\partial \chi_{x_1 \rightarrow p_1}^{(\varepsilon)}}{\partial \varepsilon} \right|_{\varepsilon=0} = \gamma (\chi_{x_1 \rightarrow x_N})^2. \quad (\text{S34})$$

At the exceptional point, i.e. $|J| = |\lambda|$ and $\varphi = \pi/2$, the susceptibility matrix can be calculated exactly analytically, see Eq. (S8). With this, we find that the responsivity at $\varepsilon = 0$ is simply given by

$$\mathcal{R} = \frac{4}{\gamma} G^{2(N-1)} = \frac{4}{\gamma} \left(4 \frac{|\lambda|}{\gamma} \right)^{2(N-1)}. \quad (\text{S35})$$

V. EFFECTS OF OPTOMECHANICAL NONLINEARITY

In our system, the detuning $g_{0,j} z_j$ due to a mechanical displacement z_j (expressed in units of the zero-point amplitude $x_{z\text{pf}}$, i.e. $z = x/x_{z\text{pf}}$) of a resonator j might be similar in magnitude to the cavity linewidth κ . In that case, the linear approximation for the Lorentzian cavity response at control laser detuning $\Delta = \kappa/(2\sqrt{3})$, which underlies the optical spring effect causing a frequency shift and facilitating interactions, becomes inadequate. This occurs generally for relatively large coherent driving, but in our experiments particularly when vibrations are amplified to

significant amplitude due to parametric amplification. It leads to deviations from linear theory that we observe in the main text. Specifically, they lead to:

- Amplitude saturation in the self-oscillation regime of main text Fig. 2, in the case of the BKC with open boundary conditions. In this regime, linear response theory breaks as it predicts a single steady state that is both dynamically and thermodynamically unstable, characterized by fluctuation eigenvalues having positive imaginary parts, and diverging average thermal energy. The figure illustrates the stabilization of the solution, a phenomenon consistent with dispersive nonlinearities and gain saturation.
- Reduced responsivity w.r.t. to the linear prediction in main text Fig. 4, especially noticeable for largest chain lengths, which exhibit the most amplification. This decrease in responsivity can be attributed to dispersive shifts and gain saturation.

In this section we discuss the basic effects of such nonlinearity, demonstrating that including higher-order terms in the optical force leads to an optically-induced effective nonlinearity in the mechanical resonators' equation of motion. The dominant effects observed align with those previously described.

A. Single resonator

Consider a single resonator dispersively coupled to an optical cavity. In the bad cavity limit, the cavity photon population induced by a drive laser with average detuning Δ adjusts (i.e., reaches its steady-state) instantaneously with position, and is given by

$$\bar{n}_c(z) = h(2[\Delta + g_0 z]/\kappa)n_{\max}, \quad (\text{S36})$$

where n_{\max} is the maximum population at resonance ($\Delta, z = 0$), and

$$h(u) = \frac{1}{1 + u^2}, \quad (\text{S37})$$

with $u = 2\Delta/\kappa$ the nondimensionalized Lorentzian cavity response function. Note that mechanical motion that is nonlinearly transduced onto the intracavity intensity generates harmonics of the mechanical oscillation in the cavity field, i.e. in the frequency spectrum of \bar{n}_c [16]. Likewise, the magnitude of the fundamental harmonic at the mechanical frequency can change non-linearly with its amplitude. The cavity field exerts a force $F_c(z) = \hbar g_0 \bar{n}_c(z)/x_{\text{zpf}}$ on the resonator, causing dynamical backaction. The fact that $\bar{n}_c(z)$ is not a linear function of z means that also the dynamical backaction has a nonlinear character. We estimate its magnitude below. Under the backaction force $f_c(z)$, the equation of motion for z reads

$$\ddot{z}(t) = -\omega^2 z(t) - \gamma \dot{z}(t) + f_c(z), \quad (\text{S38})$$

with $f_c(z) = 2\omega_0 g_0 n_{\max} h(u)$.

The standard, linear optical spring effect is obtained by expanding f_c linearly in z . As our strong control laser is detuned to induce the maximum optical spring shift ($\Delta = \kappa/(2\sqrt{3})$), the second derivative $h''(1/\sqrt{3})$ of the cavity response is zero, such that next higher order order term in the expansion of f_c is cubic in z . This leads to an effective resonator's equation of motion

$$\ddot{z}(t) \approx -\omega^2 z(t) - \gamma \dot{z}(t) - \alpha z(t)^3, \quad (\text{S39})$$

with a Duffing nonlinear coefficient

$$\alpha = \frac{8\omega g_0^4 n_{\max} h'''(2\Delta/\kappa)}{3\kappa^3} = -6\omega\delta\omega \frac{g_0^2}{\kappa^2}, \quad (\text{S40})$$

with $\delta\omega = 2g_0^2 \bar{n}_c(z=0)\Delta/(\Delta^2 + \kappa^2/4)$ and where the last expression is valid at the maximum spring shift detuning $\Delta = \pm\kappa/(2\sqrt{3})$ (corresponding to $u = \pm 1/\sqrt{3}$).

For small oscillation amplitudes A , the approximate effect of such a Duffing nonlinearity is to induce a detuning, i.e. a change of the mechanical frequency. In other words, the effect can be perceived as an effective, mechanical amplitude-dependent correction to the optical spring shift. The shifted resonance frequency μ can be found using the

Harmonic Balance method [17] to be

$$\mu^2 = \omega^2 + \frac{3\alpha}{4}A^2 \approx (\omega + \delta\omega_{\text{NL}})^2, \quad (\text{S41})$$

where ω already includes the linear spring shift $\delta\omega \ll \omega$. The nonlinear contribution to frequency shift then reads approximately

$$\delta\omega_{\text{NL}} = -\delta\omega \frac{9g_0^2}{4\kappa^2}A^2 \quad (\text{S42})$$

and counteracts the linear optical spring. Note that the factor g_0A/κ appearing in (S42) expresses the extent of the Lorentzian cavity response function (S37) that is explored by the mechanical oscillations.

B. Many resonators

As we saw above, the optomechanical nonlinearity can cause an effective correction to the optical spring effect. In multi-resonator systems, in particular when the resonators are coupled to each other through a modulated spring effect, the nonlinear effects can have various consequences. On the one hand, the effective mechanical frequency shift introduced due to nonlinearity creates an effective detuning of the affected resonator(s). On the other hand, the effective amplitudes of the couplings can change due to nonlinearity.

The displacements of multiple mechanical resonators, parametrized by $z_i = x_i/x_{\text{zpf},i}$, cause cavity frequency shifts that modulate the intracavity intensity. By applying suitable parametric driving, this effect generates BS and TMS interactions through a linear cross-spring effect, as outlined in Sec. IB and [2]. We extend the analysis of nonlinear effects in a single resonator to show that crossed nonlinearities in a resonator chain are expected under similar conditions and list the dominant contributions enhanced by modulations of the intracavity intensity. The optical force for N resonators reads

$$f_{c,i}(\mathbf{z}) = 2\omega_i n_{\text{max}} g_{0,i} n_{\text{max}} h(u(\mathbf{z})), \quad (\text{S43})$$

where we assumed the global bad-cavity limit $\omega_i \ll \kappa$, we used the shorthand $\mathbf{z} = (z_1, z_2, \dots, z_N)^T$ and made explicit that the cavity shift depends on the amplitude of all resonators $u(\mathbf{z}) = u_0 + 2 \sum_i g_{0,i} z_i / \kappa$. We now apply a perturbative expansion in the displacements $z_i \ll \kappa/g_{0,i}$, analog to that of a single resonator. In this expansion, the constant term $f_{c,i}^{(0)} = \hbar G_i n_{\text{max}} h(u_0)$ causes a shift in the resonator's equilibrium position. The first order linear correction reads

$$f_{c,i}^{(1)} = 2\omega_i g_{0,i} n_{\text{max}} \mathbf{z}^T \nabla_{\mathbf{z}} u(\mathbf{z}) = -\frac{4\omega_i g_{0,i} n_{\text{max}}}{\kappa} \sum_j g_{0,j} z_j = 0. \quad (\text{S44})$$

where $\nabla_{\mathbf{z}}$ denotes the gradient vector with respect to the \mathbf{z} coordinates. This correction recovers both self and crossed spring shift linear effects. Namely, Eq. (S44) accounts for a force exerted on resonator z_i due to a cavity modulation enacted by the oscillation of resonator z_j . This force is time-dependent, and may become resonant with the resonator i if the intracavity intensity is modulated in time: $n_{\text{max}} c_m \mapsto n_{\text{max}}(t) = n_{\text{max}} \cos(\omega_m t)$. The force is equivalent to a time-dependent interaction bilinear Hamiltonian (up to a constant term)

$$H_{\text{int}}^{(1)} = -\sum_i \int dz_i f_{c,i}^{(1)} = \sum_{i,j \neq i} \frac{t_{i,j}}{\omega_i} z_i z_j, \quad (\text{S45})$$

where $t_{i,j} = 2c_m \sqrt{3} \omega_i g_{0,i} g_{0,j} \bar{n}_c / \kappa = 2c_m \omega_i \sqrt{\delta\omega_i \delta\omega_j}$. Difference frequency modulations with $\omega_m = \omega_i - \omega_j$ (sum frequency modulation $\omega_i + \omega_j$) lead to the hopping and two-mode squeezing interactions described in the Sec. IB, with amplitudes $|J_{i,j}|, |\lambda_{i,j}| = t_{i,j}/(4\omega_i)$, recovering equations Eqs. (S1). The 2nd order term reads $f_{c,i}^{(2)} = \omega_i g_{0,i} n_r \mathbf{z}^T \mathcal{H}(\mathbf{z}) \mathbf{z}$ where $\mathcal{H}_{i,j}(\mathbf{z}) = \partial^2 h(u(\mathbf{z})) / (\partial z_i \partial z_j)$ stands for the Hessian matrix of the function $h(u(\mathbf{z}))$. This second order contribution again vanishes at the maximum spring shift operation point $\Delta = \Delta_{\pm}$ ($u_0 = u_{\pm} \equiv \pm 1/\sqrt{3}$):

$$f_{c,i}^{(2)} = \frac{8\omega_i n_r g_{0,i} (3u_0^2 - 1)}{\kappa^2 (1 + 3u_0^2)^3} \sum_{j,k} g_{0,j} g_{0,i} z_j z_k, \quad (\text{S46})$$

The third order contribution can be written succinctly as $f_{c,i}^{(3)} = \frac{\omega_i g_{0,i} n_r}{3} \sum_{j,k,l} \frac{\partial^3 h(\mathbf{u}(\mathbf{z}))}{\partial z_j \partial z_k \partial z_l} z_j z_k z_l$ and can be readily evaluated to be

$$f_{c,i}^{(3)} = - \frac{256 u_0 (u_0^2 - 1) \omega_i \bar{n}_c g_{0,i}}{\kappa^3 (u_0^2 + 1)^4} \sum_{j,k,l} g_{0,k} g_{0,k} g_{0,l} z_j z_k z_l. \quad (\text{S47})$$

At $u_0 = u_{\pm}$, the equation of motion for the amplitude z_i then reads

$$\ddot{z}_i \approx -\Omega'^2 z_i - \gamma \dot{z}_i - \sum_{j \neq i} t_{i,j} z_j - \sum_{j,k,l \neq i} \alpha_{i,j,k,l} z_j z_k z_l, \quad (\text{S48})$$

with $\alpha_{i,j,k,l} = \mp 6\sqrt{3} \omega_i \bar{n}_c g_{0,i} g_{0,j} g_{0,k} g_{0,l} / \kappa^3$.

The nonlinear contributions to this equation can be derived from a Hamiltonian

$$H_{\text{int}}^{(3)} = \frac{1}{4} \sum_{i,j,k,l} \alpha_{i,j,k,l} z_i z_j z_k z_l. \quad (\text{S49})$$

The experiment focuses on the slow evolution of mechanical resonators rotating at frequency $\omega = \omega_j$. This allows substantially simplifying Eq. (S50) by filtering out the fast dynamics via a rotating wave approximation (RWA). To apply it, we express Eq. (S49) in terms of canonical operators in a rotating frame at frequencies ω_j , leading to

$$H_{\text{int}}^{(3)} = \frac{1}{16} \sum_{i,j,k,l} \alpha_{ijkl}(t) (a_i \zeta_i + a_i^\dagger \zeta_i^*) (a_j \zeta_j + a_j^\dagger \zeta_j^*) (a_k \zeta_k + a_k^\dagger \zeta_k^*) (a_l \zeta_l + a_l^\dagger \zeta_l^*), \quad (\text{S50})$$

with $\zeta_j = e^{i\omega_j t}$. Fast-evolving contributions in the rotating frame can be averaged out, as they are assumed to only introduce perturbative corrections to the dynamics over periods $T_j = 2\pi/\omega_j$. Noting that the nonlinear coefficients $\alpha_{i,j,k,l}$ are proportional to $n_{\text{max}}(t)$ (see Eq. (S49)), the Hamiltonian comprises $(2N)^4$ terms with oscillating time-dependent prefactors. These oscillate at frequencies: $\check{\Omega}_{i,j,k,l}^m = \omega_m \pm \omega_i \pm \omega_j \pm \omega_k \pm \omega_l$.

In the optomechanical realization of the BKC, modulation frequencies are $\omega_m = \omega_i \pm \omega_j \pm \omega_k \pm \omega_l = 0, \omega_i - \omega_j$ and $\omega_i + \omega_j$. Assuming resonator frequencies do not commensurate with any frequency differences or sums, the RWA retains only the so-called *secular* terms that oscillate close to the frequency ω_j in the lab frame, where $\check{\Omega}_{i,j,k,l}^m = 0$. To filter out such contributions, we expand Eq. (S50) and express the result in normal order with the aid of a symbolic algebra software [18]: $H_{\text{int}}^{(3)} = \frac{1}{16} \sum_{i,j,k,l} H_{i,j,k,l}^{(3)}$. The contributions $H_{i,j,k,l}^{(3)}$ include corrections to resonator frequencies, hopping and squeezing interactions (two-body quadratic Hamiltonian contributions), and many-body interactions (three and four-body terms). Below, we categorize the secular contributions based on their degeneracy:

1. fourfold degeneracy $i = j = k = l$; single-body terms:

$$H_{i,i,i,i}^{(3)} \approx \frac{\alpha_{i,i,i,i}}{16} \left[12 a_i^\dagger a_i + 6 a_i^{\dagger 2} a_i^2 + 3 \right]. \quad (\text{S51})$$

Here we recover the usual form of the self-Kerr nonlinearity under the RWA.

2. threefold degeneracy $j = k = l, i \neq j$; two body terms:

$$H_{i,j,j,j}^{(3)} \approx \frac{3}{16} \alpha_{i,j,j,j} (1 + a_j^\dagger a_j) \left[\frac{c_{i,j}^-}{2} (a_i^\dagger a_j + a_j^\dagger a_i) + \frac{c_{i,j}^+}{2} (a_i a_j + a_i^\dagger a_j^\dagger) \right], \quad (\text{S52})$$

where $c_{i,j}^\pm$ are the modulation amplitudes for tones at $\omega_i \pm \omega_j$. Here we find corrections to linear coupling and squeezing, some of them assisted by the population of one of the modes — a form of nonlinear gain saturation.

3. two-fold degeneracy $k = l, i = j, i \neq k$; three-body terms:

$$H_{i,i,k,k}^{(3)} \approx \frac{\alpha_{i,i,k,k}}{16} \left[2 (a_i^\dagger a_i + a_k^\dagger a_k) + 2 a_i^\dagger a_i a_k^\dagger a_k + 1 \right]. \quad (\text{S53})$$

Here we find corrections to the spring effect and additional cross-Kerr interactions.

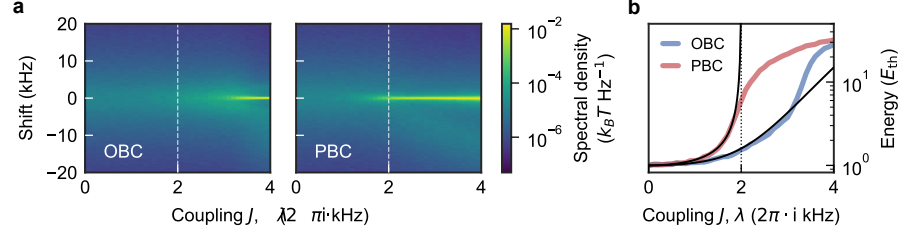


FIG. S1. **Boundary-dependent instability.** (a) Thermomechanical spectra for $J = \lambda = i\mu$ as a function of frequency and coupling strength for periodic boundary conditions (PBC) and open boundary conditions (OBC). The coupling μ is varied over a larger range than in Fig. 2 of the main text. In addition to the dynamical instability that is predicted for PBC with standard (linear) theory, we observe a dynamic instability under OBC for large values of μ that is not predicted by linear theory. Large thermal fluctuation amplitudes then induce a nonlinear detuning that generates additional gain [7], which in turn reinforces the detuning. This sets up a positive loop for the amplification, where additionally the dynamic range of the feedback cooling system may be exceeded. (b) Total thermal energy in the chain as a function of coupling strength. For large values of μ , agreement with linear theory also breaks down for OBC.

4. simple degeneracy, $k = l$, $i \neq j$, $i \neq k$, $k \neq j$; three-body terms:

$$H_{i,j,k,k}^{(3)} \approx \frac{1}{16} \alpha_{i,j,k,k} \left(1 + 2a_k^\dagger a_k \right) \left[\frac{c_{i,j}^-}{2} \left(a_i^\dagger a_j + a_j^\dagger a_i \right) + \frac{c_{i,j}^+}{2} \left(a_i a_j + a_i^\dagger a_j^\dagger \right) \right]. \quad (\text{S54})$$

5. All i, j, k, l are different: resonator frequencies do not commensurate with any sums/substraction involving 4 frequencies, so $\check{\Omega}_{ijkl}^m \neq 0$ and $H_{i,j,k,l}^{(3)} = 0$.

C. Effects of optomechanical nonlinearity on thermal populations in the presence of amplification

In Fig. 2 of the main text, we present the detected thermal fluctuations in the BKC. The theoretical predictions of the thermal populations for both open boundary conditions (OBC) and periodic boundary conditions (PBC) is provided in section III, and compared to the experimental data in Fig. 2b for varying coupling amplitudes. As we discussed above, the optomechanical nonlinearity causes a departure of the experimentally observed signal from the linear prediction at the instability that is predicted under PBC: The optomechanical nonlinearity effectively reduces the spectral content in the detected fundamental harmonic, and the mechanical self-oscillations saturate at finite amplitude that is also determined by the nonlinearity.

In contrast to the linear theory, a dynamical instability is observed under open boundary conditions for large values of μ as well. This is shown in Fig. S1, which plots the observed fluctuations for a larger range of coupling amplitudes $|J| = |\lambda| = \mu$. In that case, thermal fluctuation amplitudes that are significantly increased due to amplification induce a nonlinear detuning (V) that generates additional gain [7], which in turn reinforces the detuning. This sets up a positive loop for the amplification, where additionally the dynamic range of the feedback cooling system may be exceeded. The fact that the departures from linear theory occurs at exactly the same recorded thermal energy under both OBC and PBC further supports the hypothesis that the onset of nonlinear effects due to the amplified motion is at the root of the observed departures.

-
- [1] J. P. Mathew, J. del Pino, and E. Verhagen, Synthetic gauge fields for phonon transport in a nano-optomechanical system, *Nat. Nanotechnol.* **15**, 198 (2018).
 - [2] J. del Pino, J. J. Slim, and E. Verhagen, Non-Hermitian chiral phononics through optomechanically-induced squeezing, *Nature* **606**, 82 (2021).
 - [3] C. C. Wanjura, J. J. Slim, J. del Pino, M. Brunelli, E. Verhagen, and A. Nunnenkamp, Quadrature nonreciprocity in bosonic networks without breaking time-reversal symmetry, *Nat. Phys.* [10.1038/s41567-023-02128-x](https://doi.org/10.1038/s41567-023-02128-x) (2023).
 - [4] M. Aspelmeyer, T. J. Kippenberg, and F. Marquardt, Cavity optomechanics, *Rev. Mod. Phys.* **86**, 1391 (2014).
 - [5] M. J. Weaver, F. Buters, F. Luna, H. Eerkens, K. Heeck, S. de Man, and D. Bouwmeester, Coherent optomechanical state transfer between disparate mechanical resonators, *Nat. Commun.* **8**, 824 (2017).

- [6] A. B. Shkarin, N. E. Flowers-Jacobs, S. W. Hoch, A. D. Kashkanova, C. Deutsch, J. Reichel, and J. G. E. Harris, Optically mediated hybridization between two mechanical modes, *Phys. Rev. Lett.* **112**, 013602 (2014).
- [7] A. McDonald, T. Pereg-Barnea, and A. A. Clerk, Phase-dependent chiral transport and effective non-Hermitian dynamics in a bosonic Kitaev-Majorana chain, *Phys. Rev. X* **8**, 041031 (2018).
- [8] C. C. Wanjura, M. Brunelli, and A. Nunnenkamp, Topological framework for directional amplification in driven-dissipative cavity arrays, *Nat. Commun.* **11**, 3149 (2020).
- [9] K. Kawabata, K. Shiozaki, M. Ueda, and M. Sato, Symmetry and topology in non-Hermitian physics, *Phys. Rev. X* **9**, 041015 (2019).
- [10] P. Meystre and M. Sargent, *Elements of Quantum Optics*, 4th ed. (Springer).
- [11] F. K. Kunst, E. Edvardsson, J. C. Budich, and E. J. Bergholtz, Biorthogonal bulk-boundary correspondence in non-hermitian systems, *Phys. Rev. Lett.* **121**, 026808 (2018).
- [12] J. C. Budich and E. J. Bergholtz, Non-Hermitian topological sensors, *Phys. Rev. Lett.* **125**, 180403 (2020).
- [13] A. McDonald and A. A. Clerk, Exponentially-enhanced quantum sensing with non-Hermitian lattice dynamics, *Nat. Commun.* **11**, 5382 (2020).
- [14] J. R. Schott, *Matrix analysis for statistics* (John Wiley & Sons, 2016).
- [15] K. S. Miller, On the inverse of the sum of matrices, *Mathematics Magazine* **54**, 67 (1981).
- [16] R. Leijssen, G. La Gala, L. Freise, J. T. Muhonen, and E. Verhagen, Nonlinear cavity optomechanics with nanomechanical thermal fluctuations, *Nat. Commun.* **8**, ncomms16024 (2016), 1612.08072.
- [17] M. Krack and J. Gross, *Harmonic Balance for Nonlinear Vibration Problems* (Springer, 2019) p. 159.
- [18] J. Feist and contributors, *Quantumalgebra.jl* (2021).